

Alcohol-Soluble Conjugated Polymers Enable Highly Efficient and Stable Organic Solar Cells Through a Main-Chain Modulation Strategy

Haiyang Zhao,[#] Zixin Huang,[#] Zhibin Li, Haoran Tang,^{*} Yuanqing Bai, Hui Li, Chunchen Liu, Kai Zhang, and Fei Huang^{*}



Cite This: *Chem. Mater.* 2025, 37, 5923–5934



Read Online

ACCESS |



Metrics & More



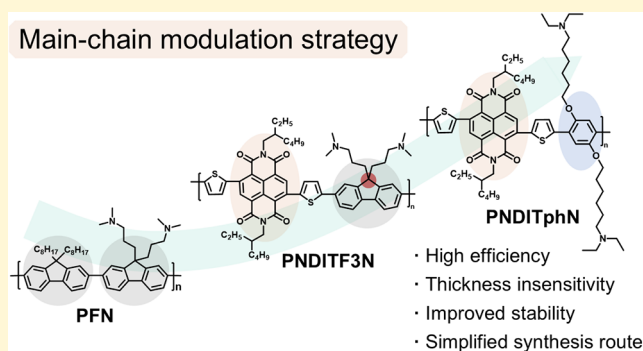
Article Recommendations



Supporting Information

ABSTRACT: Alcohol-soluble conjugated polymers have been demonstrated as effective cathode interlayer materials (CIMs) in organic solar cells (OSCs). In addition to device efficiency, stability and material preparation costs are also of critical importance. However, limited studies have focused on the intrinsic stability and synthesis procedures of CIMs. To enhance device efficiency and stability while simplifying the material synthesis process, alcohol-soluble conjugated polymers, PNDITphN and PNDITphN-Br, were synthesized through direct arylation polycondensation with precise modulation of the main-chain structures. Both polymers demonstrated superior power conversion efficiency (PCE) compared with PFN-Br. Notably, devices based on PNDITphN exhibited relatively higher PCE than those based on PNDITphN-Br, attributed to its face-on molecular packing, more uniform surface morphology, and stronger interfacial contact with the active layer. As a result, ternary devices using PNDITphN and PNDITphN-Br achieved maximum PCEs of 18.84% and 18.36%, respectively. Moreover, PNDITphN-based devices enhanced light stability compared to those based on PFN-Br and PNDITF3N. These findings provide new insights into cathode interlayer engineering for achieving highly efficient and stable OSCs.

Main-chain modulation strategy



INTRODUCTION

In recent years, organic solar cells (OSCs) have attracted considerable attention owing to their advantages of physical lightweight, mechanical flexibility, and solution processability.^{1–7} Currently, the power conversion efficiency (PCE) of single-junction OSCs has surpassed 20%,^{8–11} which basically meets the demand of commercial applications. This rapid progress in efficiency is attributed to advances in both device optimizations^{12–14} and material innovations,^{15–18} including active layer and interfacial layer materials.^{19–27} In a multilayer OSC structure, the active layer absorbs photons, generating excitons that dissociate into free carriers, which are then transported through the interfacial layers to the electrodes for collection. The cathode interlayer (CIL) plays a crucial role in lowering the work function (WF) of the electrode, facilitating ohmic contact between the active layer and the metal electrode, thereby enhancing charge extraction, transport, and collection.²⁸ In addition, the CIL protects the active layer by preventing metal atom migration during electrode deposition²⁹ and blocking water and oxygen penetration,³⁰ significantly improving the stability. Therefore, the rational design of cathode interface materials (CIMs) is critical for enhancing both the efficiency and the long-term stability of OSC devices.

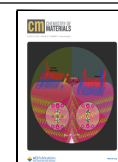
In general, CIMs can be categorized into inorganic and organic materials. Inorganic CIMs, particularly transition metal oxides, are widely used in CILs due to their excellent charge transport properties, such as zinc oxide (ZnO),³¹ tin oxide (SnO₂),³² and titanium dioxide (TiO₂).³³ While inorganic metal oxides are commonly employed in inverted devices, organic water/alcohol materials present a promising alternative in conventional devices.³⁴ Organic CIMs can be subdivided into conjugated small molecules and conjugated polymers. PDI- and NDI-based conjugated small molecules have been developed, such as PDINO,³⁵ PDINN,³⁶ PDI-M,³⁷ NDIO,³⁸ NDI-Br,³⁹ and NDI-ph.⁴⁰ Compared with conjugated small molecules, conjugated polymers offer improved film-forming properties. A representative example is conjugated polymer PFN, which contains a conjugated main chain and polar side chains, enabling water/alcohol processing and improving

Received: May 16, 2025

Revised: July 18, 2025

Accepted: July 21, 2025

Published: July 28, 2025



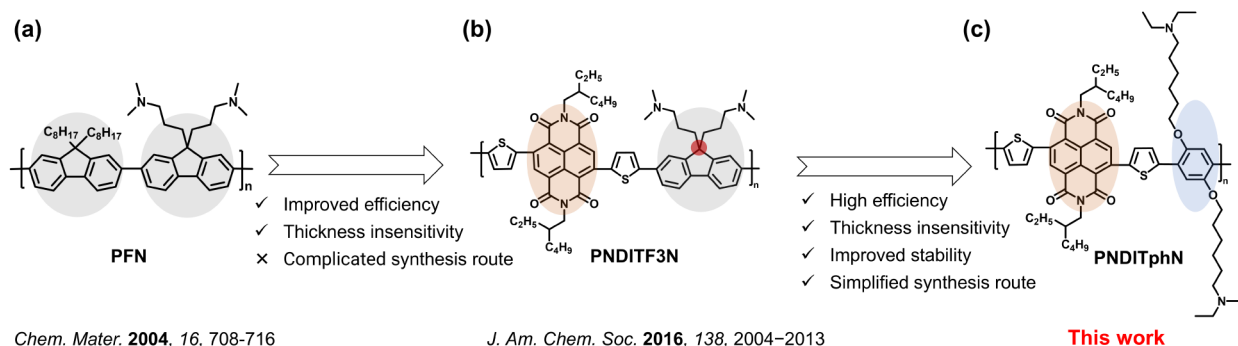
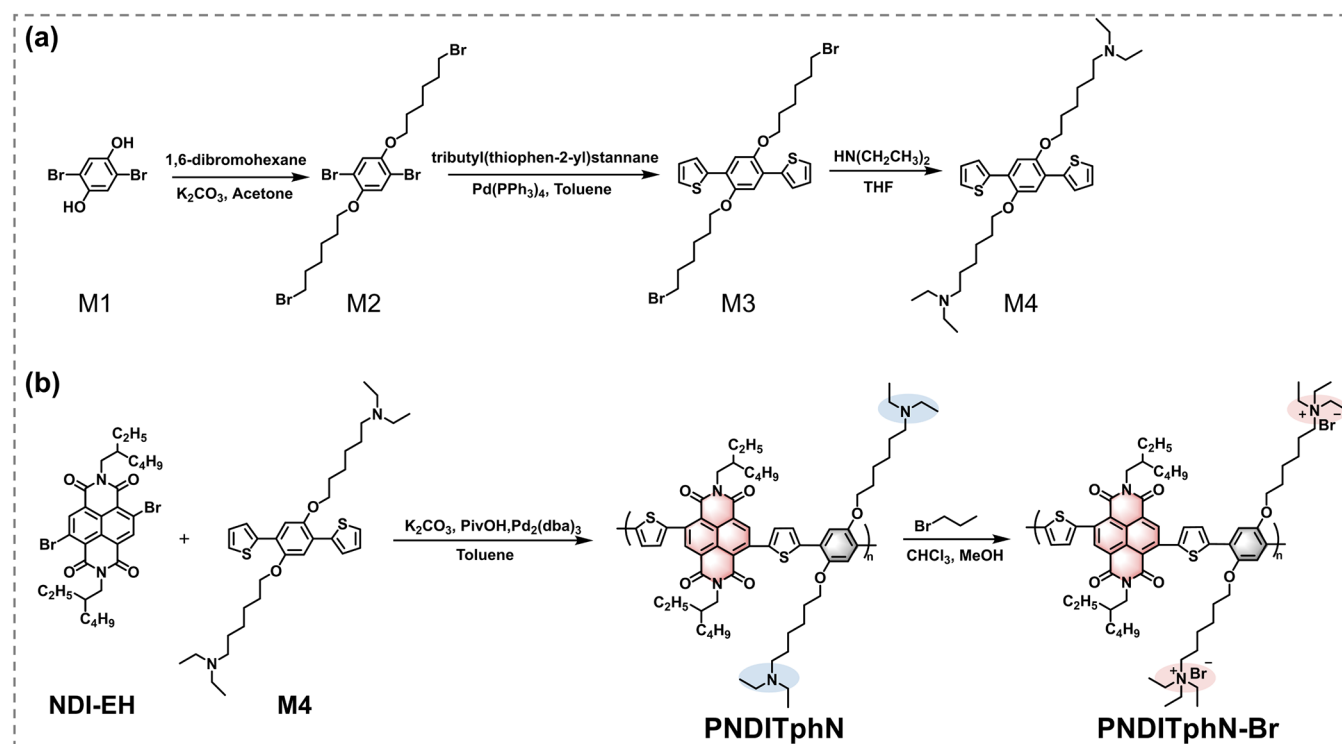


Figure 1. Conjugated polymer design strategies: retain the acceptor unit and replace the donor fluorene unit. Chemical structures of (a) PFN, (b) PNDITF3N, and (c) PNDITphN.

Scheme 1. Synthetic Routes of the Monomers and the Polymers PNDITphN and PNDITphN-Br



device efficiency.⁴¹ Subsequently, polyfluorene-based water/alcohol-soluble conjugated materials have been extensively developed for CIL applications.^{42–45} However, due to their low electron mobility, polyfluorene-based CIMs are effective only in ultrathin films, which restricts their broader application. To address this limitation, an electron-deficient NDI unit was introduced into the polymer, resulting in PNDITF3N that functions effectively as a cathode interlayer in thicker films.⁴⁶ Up to now, PNDITF3N has been applied in high-efficiency OSC devices widely,⁴⁷ and then a series of CIMs based on electron-deficient units have been developed.^{18,48,49} However, limited studies have focused on the intrinsic stability and the synthesis procedure of CIMs, which are of importance for the commercialization of OSCs. It has been reported that conjugated polymers containing fluorene units demonstrated poor light stability.^{50,51} Additionally, the predominant reliance on Stille or Suzuki coupling methods for most CIM synthesis involves complex synthetic protocols, presenting a significant barrier to OSC industrialization. Therefore, designing high-

performance polymer-based CIMs with enhanced efficiency and stability and developing simplified synthesis methods are crucial for promoting the development of OSCs.

In this study, we developed two alcohol-soluble polymers by precisely modulating the conjugated main-chain structure. As depicted in Figure 1, the target polymer PNDITphN was synthesized through direct arylation polycondensation (DARP) by strategically retaining the electron-deficient NDI unit while substituting the fluorene moiety with a benzene ring. This methodology eliminates the requirement for toxic organotin reagents or borates, thereby simplifying the synthetic protocol. The ionic side chain-based polymer PNDITphN-Br was obtained by treating PNDITphN with excess bromoethane. Owing to the introduction of electron-deficient unit NDI, OSC devices based on these two polymeric CIMs achieved higher PCE than the traditional PFN-Br-based devices. However, it was found that their aggregation behaviors differed significantly. PNDITphN-Br exhibited stronger aggregation, resulting in a rougher surface morphology, which is detrimental to

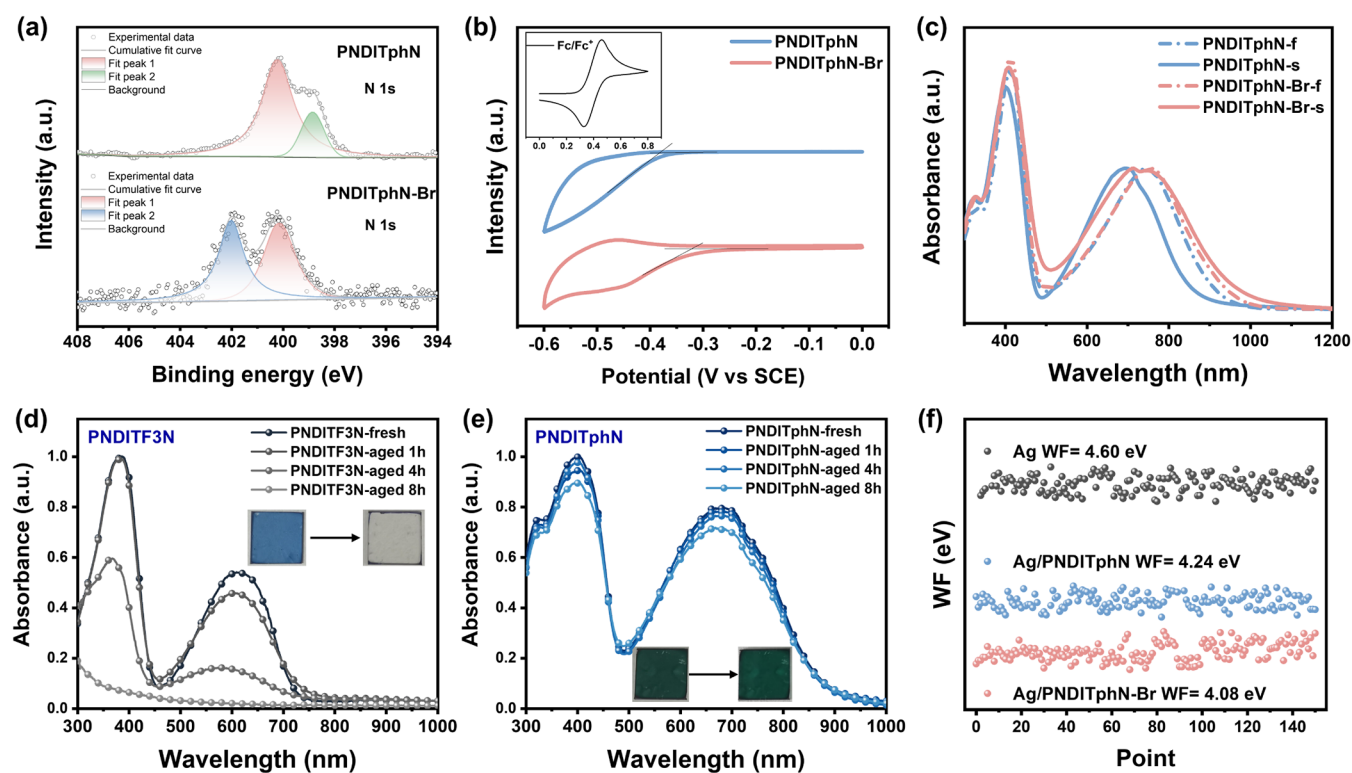


Figure 2. (a) N 1s signal of XPS spectra of PNDITphN and PNDITphN-Br; (b) cyclic voltammograms of polymers; (c) UV–vis–NIR absorption spectra of the polymers in the thin film state and in methanol solution; the time-dependent UV–vis absorption spectra of the polymer: (d) PNDITF3N and (e) PNDITphN; (f) KPFM spectra of PNDITphN, PNDITphN-Br, and bare Ag.

Table 1. Summary of the Electrochemical Properties of the Two Polymers

| Polymer | $\lambda_{\text{onset}}^{\text{sol}}$ (nm) | $\lambda_{\text{onset}}^{\text{film}}$ (nm) | $E_{\text{g}}^{\text{opt}}$ (eV) | $E_{\text{LUMO}}^{\text{b}}$ (eV) | $E_{\text{HOMO}}^{\text{c}}$ (eV) |
|-------------|--|---|----------------------------------|-----------------------------------|-----------------------------------|
| PNDITphN | 916 | 860 | 1.44 | −4.05 | −5.49 |
| PNDITphN-Br | 945 | 968 | 1.28 | −4.11 | −5.39 |

$^{\text{a}}E_{\text{g}}^{\text{opt}} = 1240/\lambda_{\text{onset}}^{\text{film}}$. $^{\text{b}}E_{\text{LUMO}} = -(4.80 + E_{\text{onset}}^{\text{red}})$ eV. $^{\text{c}}E_{\text{HOMO}} = (E_{\text{LUMO}} - E_{\text{g}}^{\text{opt}})$ eV.

charge transport. Surface energy measurements further revealed that PNDITphN's surface energy more closely matched that of the active layer materials, resulting in tighter interfacial contact, reduced defect and trap density, and improved charge transfer from the active layer to the CIL. Consequently, binary and ternary OSC devices using PNDITphN-based CIL achieved maximum PCEs of 18.39% and 18.84%, higher than 17.78% and 18.36% for PNDITphN-Br-based devices. Moreover, PNDITphN-based devices exhibited better photostability than those using PFN-Br and PNDITF3N, highlighting their potential for future commercial applications. These findings offer new insights into cathode interlayer engineering for improving the efficiency and stability of OSCs.

RESULTS AND DISCUSSION

Synthesis and Characterization. The synthetic routes for PNDITphN and PNDITphN-Br are outlined in [Scheme 1](#). Monomer M1 was purchased from a commercial source, while M2 was obtained by reacting M1 with an excess of 1,6-dibromohexane. M2 was then subjected to Stille coupling with tributyl(thiophen-2-yl)stannane, yielding M3. Subsequently, M3 was treated with diethylamine to afford the target compound M4, featuring tertiary amine neutral side chains. NDI-EH was synthesized by following a previously reported

approach. Detailed synthetic procedures for all monomers are provided in the [Supporting Information](#), and their structures were confirmed via ^1H and ^{13}C NMR.

The target neutral side-chain-based conjugated polymer, PNDITphN, was synthesized via DARp. This method enables direct C–C bond formation without the use of toxic organotin reagents, simplifying the synthesis and making it more suitable for industrial applications. The number-average molecular weight (M_n)/polymer dispersity index (PDI) of PNDITphN was determined to be 7.7 kDa/2.97 via gel permeation chromatography (GPC) using chloroform as the eluent ([Figure S3](#)). PNDITphN was treated with excess bromoethane in darkness for 4 days, yielding the ionic side-chain-based conjugated polymer PNDITphN-Br. X-ray photoelectron spectroscopy (XPS) was conducted to confirm the successful ionization of the side chains. As shown in [Figure 2a](#), the N 1s peaks at 400.2 and 398.8 eV of PNDITphN could be assigned to the imide of the NDI unit and tertiary amine groups on the side chains, respectively. In PNDITphN-Br, the imide peak remains, but the peak for the tertiary amine groups disappears, and a new N 1s peak at 402.0 eV, corresponding to quaternary ammonium (N^+) groups, appears. These results confirm the transition from neutral to quaternary ammonium side chains. PNDITphN is soluble in common organic solvents like chloroform, toluene, and chlorobenzene and can also dissolve

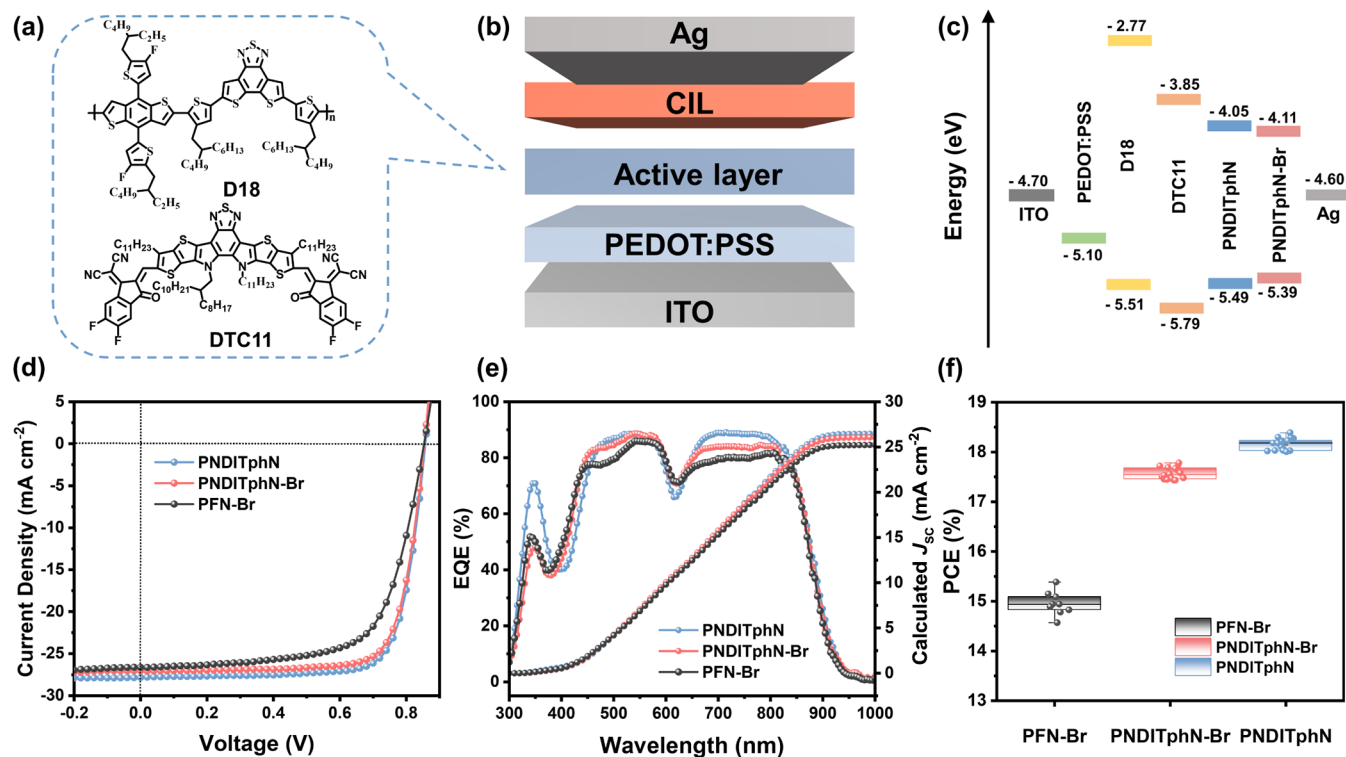


Figure 3. (a) Chemical structures of D18 and DTC11; (b) device structure with ITO/PEDOT:PSS/active layer/CILs/Ag; (c) energy level diagram; (d) J - V curves of devices with different CIMs; (e) EQE curves of devices with different CIMs; (f) Box plots of PCEs of devices based on CIMs of PFN-Br, PNDITphN, or PNDITphN-Br.

Table 2. Photovoltaic Performance of D18:DTC11-Based OSCs with Different CIMs

| CIMs | V_{OC} (V) | J_{SC} (mA cm^{-2}) | J_{cal}^a (mA cm^{-2}) | FF (%) | PCE_{max}/PCE_{ave}^b (%) |
|-------------|---------------------------|----------------------------------|-------------------------------------|--------------------------|-----------------------------|
| PNDITphN | 0.857 (0.859 \pm 0.002) | 27.84 (27.68 \pm 0.19) | 26.45 | 77.06 (76.36 \pm 0.50) | 18.39 (18.16 \pm 0.12) |
| PNDITphN-Br | 0.854 (0.855 \pm 0.004) | 27.06 (27.19 \pm 0.17) | 26.08 | 76.94 (75.60 \pm 0.69) | 17.78 (17.57 \pm 0.12) |
| PFN-Br | 0.856 (0.857 \pm 0.003) | 26.46 (26.12 \pm 0.47) | 25.23 | 68.29 (67.05 \pm 0.78) | 15.48 (15.00 \pm 0.20) |

^aIntegrated from EQE curves. ^bThe average PCE was obtained from at least 10 independent devices.

in methanol (>10 mg/mL) with the aid of 1% acetic acid. In contrast, PNDITphN-Br is completely insoluble in common solvents but exhibits excellent solubility in methanol (>15 mg/mL). The alcohol solubility of both polymers allows for orthogonal solvent processing, ensuring the active layer remains intact when depositing the cathode interlayer.

Thermogravimetric analysis (TGA) and differential scanning chromatography (DSC) were conducted to investigate the thermal behavior of PNDITphN and PNDITphN-Br. As shown in Figure S4, the thermal decomposition (T_d) temperature (5% loss) of PNDITphN and PNDITphN-Br was determined to be 332 and 215 °C, respectively. The lower T_d of PNDITphN-Br is attributed to the decomposition of the ethyl bromide group in the quaternary ammonium salts.⁵² When the temperature rises to about 300 °C, both of the polymers continue to decompose due to the decomposition of the tertiary amine groups. The side chains start to decompose as the temperature continues to increase. No significant phase transition peaks were observed in the DSC spectra before T_d (Figure S4).

Electrochemical and Optical Properties. The lowest unoccupied molecular orbital (LUMO) levels of both polymers were measured by the cyclic voltammetry method. As shown in Figure 2b, both polymers showed obvious redox processes, and the LUMO energy levels of PNDITphN and

PNDITphN-Br were calculated to be -4.05 and -4.11 eV, respectively, based on the onsets of reduction peaks. The electron-deficient NDI units in the conjugated backbone enable the low LUMO energy levels. Notably, Y-series acceptor molecules typically have LUMO energy levels around -4.0 eV, and the low LUMO levels of the cathode interlayer materials can overcome the energy barrier, facilitating efficient electron transport.

The optical properties of PNDITphN and PNDITphN-Br were characterized by UV-vis-NIR absorption spectroscopy in a methanol solution and thin films. As shown in Figure 2c, both of polymers exhibit two similar main absorption bands. The first peak at 350–450 nm is attributed to the absorbance of π - π^* transition in the polymer main chain, and the broad band at the lower-energy region is attributed to the intramolecular charge transfer (ICT) from the electron-rich units to the electron-deficient NDI unit. Compared with the neutral PNDITphN, PNDITphN-Br shows a slight red shift in solution absorption, possibly due to electrostatic perturbation, the polar solvent effect, or multichain aggregation.⁵³ In the thin-film state, the absorption onsets for PNDITphN and PNDITphN-Br are at 860 and 968 nm, respectively. This corresponds to optical bandgap energies (E_g^{opt}) of 1.44 and 1.28 eV for PNDITphN and PNDITphN-Br, respectively. The highest occupied molecular orbital (HOMO) levels of

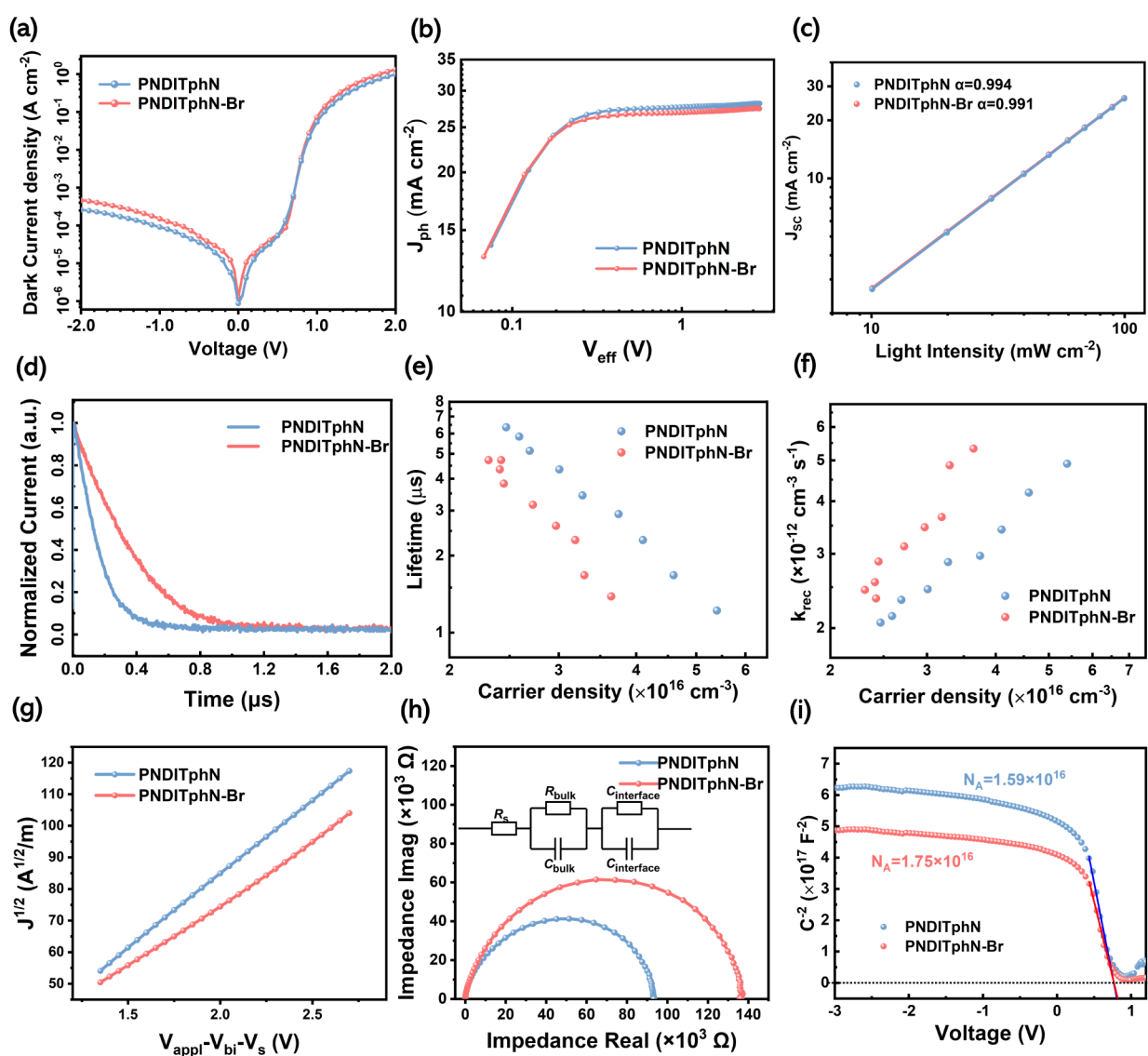


Figure 4. (a) Dark current vs voltage curves; (b) $J_{\text{ph}}-V_{\text{eff}}$ curves of two devices; (c) light intensity dependence of J_{SC} ; (d) normalized transient photocurrent traces of devices; (e) carrier lifetime versus carrier density of two devices; (f) bimolecular recombination rate constants (k_{rec}) versus carrier density of two devices; (g) SCLC measurement for bilayer electron-only devices; (h) impedance spectra of the devices and the equivalent circuit model; (i) $C^{-2}-V$ curves and Mott–Shockley plots.

PNDITphN and PNDITphN-Br were calculated to be 5.49 and 5.39 eV from the optical bandgap, respectively. Specifically, PNDITphN-Br shows a clear red shift of approximately 100 nm compared to PNDITphN (Figure 2c and Table 1). This red shift in the absence of solvent is likely due to electrostatic interactions and changes in aggregation. The result indicates that the shift from neutral to ionic side chains significantly affects the aggregation behavior of the conjugated polymer.

Photostability Investigation. To validate our design strategy, the effect of changing the fluorene unit into the benzene unit on photostability, we examined the changes in the absorption spectra of PFN, PNDITF3N, and PNDITphN films following equal durations of UV irradiation. As depicted in Figure S5, PFN exhibits the poorest photostability, as it no longer displays a characteristic absorption peak after 10 min of UV light irradiation. As shown in Figure 2d, after 1 h of UV irradiation, the absorption around 620 nm for PNDITF3N films diminished to 84.8% of its initial intensity. With extended

exposure, the absorption peak continued to decline, reaching 29.6% after 4 h and becoming nearly undetectable after 8 h, as also evidenced by the photo of the film. On the contrary, the films of PNDITphN showed better UV stability. As shown in Figure 2e, the degradation of PNDITphN films was minimal, with the absorption peak at 680 nm retaining 96.0% of its initial intensity after 1 h and 90.4% after 8 h of UV irradiation. The above results effectively verified that the UV stability of the conjugated polymer could be significantly enhanced by modifying the polymer backbone and substituting the fluorene unit with a benzene unit.

Work Function Adjustment Capability. The work function (WF) of the metal electrode plays a critical role in charge extraction and collection. In the absence of a charge injection layer (CIL), a Schottky contact is likely to form between the active layer and the electrode, resulting in the formation of a space charge region at the interface, which impedes electron transport from the active layer to the electrode. Therefore, it is important to regulate the WF of the

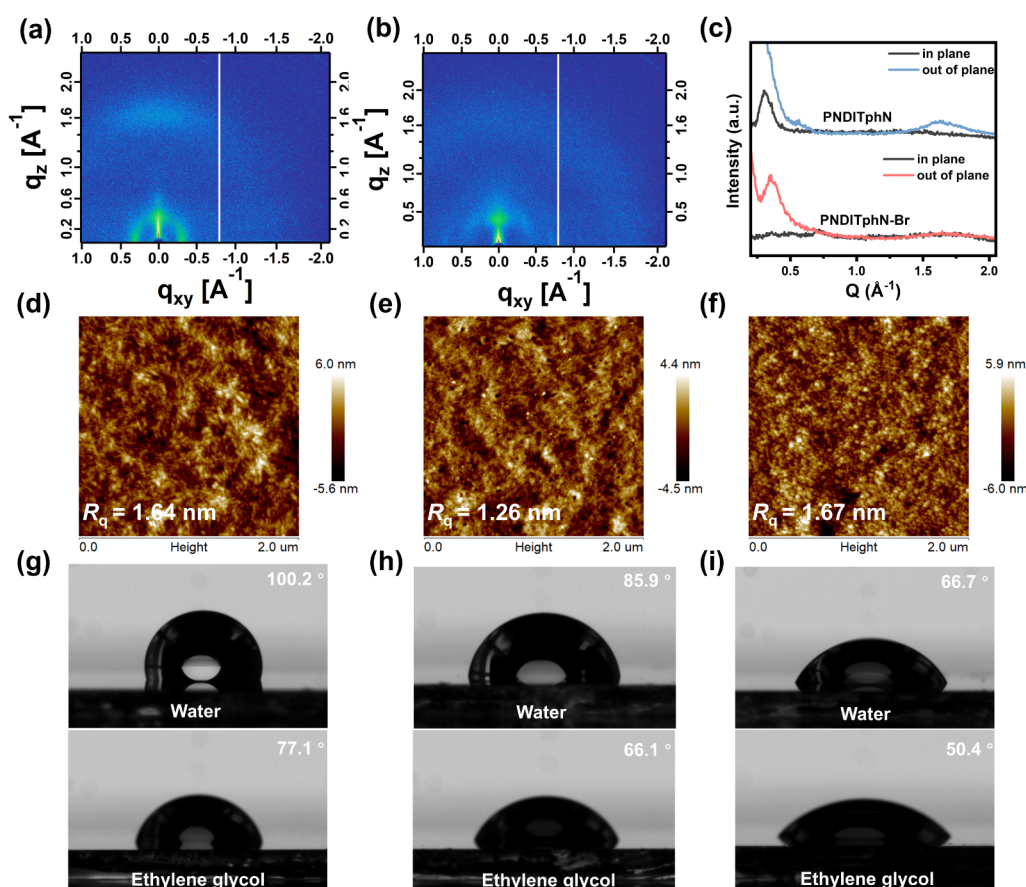


Figure 5. 2D GIWAXS images of (a) PNDITphN, (b) PNDITphN-Br; (c) corresponding 1D profiles of in-plane and out-of-plane directions of the polymers; AFM height images of (d) bare active layer film, (e) PNDITphN and (f) PNDITphN-Br films deposited on the active layer; contact angle images of water and ethylene glycol of (g) bare active layer films, (h) PNDITphN, and (i) PNDITphN-Br films deposited on the active layer.

electrode to form an Ohmic contact between the active layer and the electrode by introducing a CIL. Kelvin probe microscopy (KPM) was conducted to measure the WF values of the Ag electrode modified by PNDITphN or PNDITphN-Br. As shown in Figure 2f, the WF of bare Ag (4.60 eV) was reduced to 4.24 eV after spin-coating PNDITphN and to 4.08 eV after spin-coating PNDITphN-Br. The result indicates that both of these polymers could reduce the WF of the electrode effectively, and CILs based on quaternary ammonium salt side chains form a larger interfacial dipole compared to those based on neutral tertiary amine side chains, consistent with previous reports.⁴⁶

Photovoltaic Performance. To evaluate the performance of PNDITphN and PNDITphN-Br as CIMs, nonfullerene OSCs were fabricated with a conventional structure of ITO/PEDOT:PSS/D18:DTC11/CIMs/Ag. The chemical structures of D18 and DTC11, along with the device structure, are depicted in Figure 3a,b. For comparison, OSC devices incorporating PFN-Br as the CIM were also fabricated. The energy levels of active layer materials and CIMs are depicted in Figure 3c. The LUMO levels of PNDITphN and PNDITphN-Br are lower than that of the acceptor DTC11, which is beneficial for the charge transfer from the active layer to the cathode electrode. The current density–voltage (J – V) characteristics and external quantum efficiency (EQE) spectra are shown in Figure 3d,e, and the photovoltaic parameters are summarized in Table 2. The devices employing PNDITphN, PNDITphN-Br, and PFN-Br (5 nm) as CIMs achieved

maximum PCEs of 18.39%, 17.78%, and 15.48%, respectively. Furthermore, as shown in Figure S6, the PCE of devices with a PFN-Br interlayer decreased significantly with increasing film thickness. In contrast, devices using PNDITphN and PNDITphN-Br maintained over 80% of their initial efficiency, even when the film thickness was increased to 25 nm, highlighting the potential of these materials for industrial-scale applications. This improvement in efficiency validates the strategy of incorporating electron-deficient units into the conjugated skeleton. Additionally, Figure 3f shows that PNDITphN-based devices achieved higher average efficiencies compared to PNDITphN-Br-based devices. A detailed analysis of the fill factor (FF) and current density (J_{SC}) reveals that PNDITphN-based devices reached a J_{SC} of 27.68 mA cm⁻² and an FF of 76.36%, both higher than the 27.19 mA cm⁻² J_{SC} and 75.60% FF of PNDITphN-Br-based devices, resulting in a higher PCE. This difference will be discussed in more detail later in this article.

Charge Transport, Extraction, and Recombination.

To further understand the differing device performance of OSCs using the CIM of PNDITphN or PNDITphN-Br, the charge transport characteristics of devices have been carefully investigated. Both PNDITphN- and PNDITphN-Br-based devices exhibited low reverse saturation current density in the dark (Figure 4a), indicating effective interface modification between the active layer and the metal electrode, which is beneficial for suppressing leakage current. The relationship between the photocurrent density (J_{ph}) and effective voltage

Table 3. Photovoltaic Performance of the OSCs Based on These Two CIMs with Different Active Layers^a

| Active layer | CIMs | V_{OC} (V) | J_{SC} (mA cm ⁻²) | J_{cal} (mA cm ⁻²) | FF (%) | PCE _{max} /PCE _{ave} ^b (%) |
|---------------|-------------|-----------------------|---------------------------------|----------------------------------|----------------------|---|
| PM6:Y6 | PNDITphN | 0.846 (0.843 ± 0.002) | 27.16 (27.48 ± 0.27) | 26.13 | 77.41 (76.30 ± 1.17) | 17.78 (17.67 ± 0.20) |
| | PNDITphN-Br | 0.842 (0.843 ± 0.002) | 26.93 (27.09 ± 0.14) | 25.98 | 75.98 (75.21 ± 0.91) | 17.22 (17.18 ± 0.18) |
| PM6:D18:L8-BO | PNDITphN | 0.889 (0.889 ± 0.001) | 26.54 (26.59 ± 0.09) | 25.30 | 79.86 (79.39 ± 0.47) | 18.84 (18.77 ± 0.11) |
| | PNDITphN-Br | 0.884 (0.883 ± 0.001) | 26.00 (26.13 ± 0.11) | 24.93 | 79.89 (78.63 ± 1.11) | 18.36 (18.13 ± 0.20) |

^aThe device structure is ITO/PEDOT:PSS/active layer/CIMs/Ag. ^bThe average PCE was obtained from at least 6 independent devices.

(V_{eff}) was measured in order to understand the charge generation and dissociation process in devices. J_{ph} is calculated as $J_{ph} = J_{light} - J_{dark}$ in which J_{light} is the current density under illumination and J_{dark} is the current density in the dark. V_{eff} is defined as $V_{eff} = V_0 - V_{appl}$, where V_0 is the corresponding voltage when $J_{ph} = 0$ mA cm⁻², and V_{appl} is the applied voltage bias. Ideally, when the voltage is large enough, all photo-generated excitons will dissociate into free carriers and then be collected by the electrodes. As shown in Figure 4b, the photocurrent density increased linearly with voltage and eventually saturated, reaching the saturation current density (J_{sat}), which can be used to estimate the charge generation of the devices. Devices based on PNDITphN and PNDITphN-Br achieved a J_{sat} of 28.14 and 27.48 mA cm⁻², respectively, indicating more efficient charge generation in the PNDITphN-based device. The exciton dissociation probability (P(E,T)), defined as J_{ph}/J_{sat} , was also calculated. The P(E,T) value for the PNDITphN-based device was 98.12%, higher than 97.74% for the PNDITphN-Br-based device, indicating that the neutral side chain-based PNDITphN promotes more efficient exciton generation and dissociation, leading to a higher FF.

In addition to the charge extraction process, the dependence of J_{SC} on the light intensity (P_{light}) was examined to explore charge recombination dynamics. The relationship follows $J_{SC} \propto P_{light}^\alpha$, where the α value represents the degree of bimolecular recombination, with an α close to 1 indicating minimal recombination. As shown in Figure 4c, the α values for PNDITphN- and PNDITphN-Br-based devices were 0.994 and 0.991, respectively. The slightly higher α value suggests a better suppression of bimolecular recombination in PNDITphN-based devices.

Transient photocurrent (TPC) and transient photovoltage (TPV) measurements were further conducted to measure the carrier extraction time and carrier lifetime in these devices. As shown in Figure 4d, the charge extraction time for the device with PNDITphN-Br is 0.29 μ s, while it decreases to 0.14 μ s for the device with PNDITphN, indicating superior carrier extraction in the latter. The TPV results (Figure S7) reveal that the carrier lifetime for the PNDITphN-based device is 35.71 μ s, which is significantly longer than the 18.34 μ s observed for the PNDITphN-Br-based device. The longer carrier lifetime could be attributed to smoother morphology and reduced recombination, as demonstrated in the previous tests. Additionally, Figure S8a shows that the PNDITphN-based device exhibits a longer carrier lifetime (τ) across the entire V_{OC} range compared to that of the PNDITphN-Br-based device. The carrier density (n) was further measured by the carrier extraction (CE) technique, with n versus V_{OC} plotted in Figure S8b. The results indicate that the PNDITphN-based device consistently achieves higher n values across the entire V_{OC} range, aligning with the observed enhancement in the J_{SC} . The derived carrier lifetime curves under different carrier densities are shown in Figure 4e. The bimolecular recombination rate constants (k_{rec}) can be extracted from the carrier lifetime and carrier density according to the formula: $k_{rec} = 1/(\lambda + 1)n\tau$, where λ is the recombination order from Figure 4e. The plot of k_{rec} versus n is shown in Figure 4f, and it is found that the k_{rec} values of the PNDITphN-based device are significantly lower than those of the PNDITphN-Br-based device at all V_{OC} ranges, indicating a lower degree of bimolecular recombination and improved FF, consistent with previous findings. Consequently, the electron mobility (μ_e) was measured by the bilayer

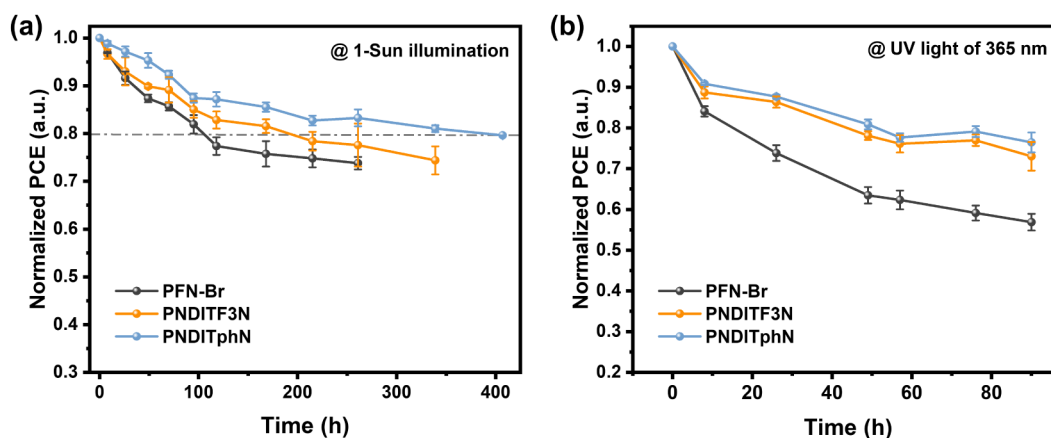


Figure 6. PCE variation diagrams of devices based on polymer PFN-Br, PNDITF3N, and PNDITphN under (a) AM1.5 sunlight and (b) 365 nm ultraviolet light illumination.

electron-only device structure of ITO/ZnO/DTC11/CIMs/Ag, and the results were fitted by the space charge limited current (SCLC) method. As shown in Figure 4g, the PNDITphN-based device demonstrates a higher μ_e of $8.42 \times 10^{-4} \text{ cm}^2 \text{ V}^{-1} \text{ s}^{-1}$ compared to $5.57 \times 10^{-4} \text{ cm}^2 \text{ V}^{-1} \text{ s}^{-1}$ for the PNDITphN-Br-based device. This higher electron mobility can be attributed to faster carrier extraction, longer carrier lifetime, and reduced carrier recombination in the PNDITphN-based device. Moreover, the charge transport property was also explored by electrochemical impedance spectroscopy (EIS). As shown in Figure 4h, the EIS curves were fitted using the model with a bulk recombination resistance (R_{bulk}), carrier transport resistance (R_{tran}), and series resistance (R_{series}), and the relevant parameters are summarized in Table S3. The results indicate that the PNDITphN-based device exhibits lower resistance compared to the PNDITphN-Br-based device, suggesting that the neutral side chains of PNDITphN facilitate better carrier extraction. This can be attributed to weaker aggregation and fewer interfacial defects of PNDITphN from the UV-vis spectra. Altogether, these findings demonstrate that PNDITphN-based devices exhibit superior charge transfer characteristics, resulting in higher J_{SC} and FF.

To further investigate the different charge recombination of these two devices, the capacitance–voltage (C – V) measurements and Mott–Schottky analysis were conducted to study the trap density.^{54,55} Trap states can capture electrons or holes, thus affecting the electrical property. The trapped charge density (N_A) was calculated using eq 1.

$$N_A = \frac{-2}{q\epsilon_0\epsilon_r A^2 k} \quad (1)$$

where q is the elementary charge, ϵ_0 is the vacuum permittivity, ϵ_r is the relative dielectric constant, A is the device area, and k is the slope of the linear regime in the C^{-2} – V curve as shown in Figure 4i. The PNDITphN-based devices exhibit a trap density of $1.59 \times 10^{16} \text{ cm}^{-3}$, smaller than $1.76 \times 10^{16} \text{ cm}^{-3}$ of PNDITphN-Br-based devices. Furthermore, capacitance–frequency (C – ω) measurement was conducted to explore the density distribution of trap states. The trap density of states distribution $N_T(E_\omega)$ refers to the number distribution of defect states in the unit energy range. The trap energy E_ω and frequency ω are defined by the following equation:

$$E_\omega = k_B T \ln\left(\frac{\omega_0}{\omega}\right) \quad (2)$$

The trap density of states distribution $N_T(E_\omega)$ is defined by eq 3.

$$N_T(E_\omega) = \frac{\beta}{qAd} \frac{V_{\text{bi}}}{k_B T} \frac{\omega dC}{d\omega} \quad (3)$$

where k_B is the Boltzmann's constant, T is the temperature, V_{bi} is the built-in potential, d is the total thickness of the interlayer and the active layer, β is a small correction factor ≈ 1 , and ω_0 is the rate prefactor for thermal excitation from the trap, which is approximately 10^{12} s^{-1} in OSCs.⁵⁶ The state density distribution curves of the corresponding devices under different trap energies are plotted in Figure S9. The devices based on PNDITphN and PNDITphN-Br exhibited trap densities of states of $6.93 \times 10^{16} \text{ cm}^{-3} \text{ eV}^{-1}$ and $8.55 \times 10^{16} \text{ cm}^{-3} \text{ eV}^{-1}$, respectively. The slightly lower N_T of PNDITphN-based devices indicated a decreased possibility of recombination and thus a better carrier transport property. The results are consistent with the longer carrier lifetime and higher electron mobility of PNDITphN, resulting in higher J_{SC} and FF values for PNDITphN-based devices.

Molecular Packing and Surface Morphological Characteristics. To further investigate the reasons for the different charge transport behaviors of PNDITphN and PNDITphN-Br, grazing-incidence wide-angle X-ray scattering (GIWAXS) and atomic force microscopy (AFM) were performed. In GIWAXS spectra of the PNDITphN film (Figure 5a,c), an obvious π – π stacking peak located at 1.641 \AA^{-1} (010) diffraction was observed in the out-of-plane direction, alongside a lamellar structure signal at 0.314 \AA^{-1} (100) diffraction in the in-plane direction, indicating a face-on molecular orientation, which is favorable for carrier transport in the vertical direction.⁵⁷ Conversely, the PNDITphN-Br film (Figure 5b,c) exhibited only a weak (010) peak in the out-of-plane direction, with a pronounced (100) lamellar structure signal, suggesting an edge-on molecular orientation.

Thin film morphology of the two CIMs (5 nm) deposited on the active layer was measured by AFM. As shown in Figure 5d, the bare active layer without CIMs exhibits a fiber structure and has a root-mean-square (RMS) roughness of 1.64 nm. After depositing PNDITphN and PNDITphN-Br on the active layer, PNDITphN-Br exhibits an islet-like morphology, while

PNDITphN exhibits a relatively smoother surface. The RMS roughness values for PNDITphN and PNDITphN-Br are 1.26 and 1.67 nm, respectively (Figure 5e,f). In addition, as shown in Figure S10, conjugated polymer films with a thickness of approximately 50 nm were deposited for the measurements. The root-mean-square (RMS) roughness values for PNDITphN and PNDITphN-Br were 1.92 and 3.84 nm, respectively, indicating that PNDITphN has a smoother surface, while PNDITphN-Br exhibits an island-like morphology and a rougher surface. The lower RMS value of PNDITphN is advantageous for minimizing interfacial defects and trap density, thereby reducing carrier recombination. These findings suggest that PNDITphN-Br undergoes stronger aggregation after ionization of the neutral side chains in PNDITphN. These results imply that PNDITphN favors face-on molecular packing with moderate aggregation, while PNDITphN-Br prefers edge-on packing and exhibits stronger aggregation, which is unfavorable for charge transport.

Furthermore, to assess the compatibility between the active layer and CIMs, the contact angles of water and ethylene glycol (EG) on the bare active layer and CIMs-deposited layers were measured. The contact angle images are shown in Figure 5g–i, with corresponding results summarized in Table S4. The pure D18:DTC11 film exhibits hydrophobic characteristics with a large contact angle, which decreases after the deposition of the interfacial layers. Notably, the contact angle of PNDITphN is closer to that of the bare active layer, promoting a denser contact between the active layer and the interlayer. Surface free energy (γ) values for the bare active layer, PNDITphN, and PNDITphN-Br were calculated using the Owens–Wendt model.⁵⁸ The surface energy values of the bare active layer, PNDITphN, and PNDITphN-Br are 20.87, 23.73, and 35.45 mN m⁻¹, respectively (Table S4). A large difference in surface energy between layers typically hinders the formation of tight interfacial contact. Therefore, the carriers in the device with PNDITphN-Br are more likely to recombine at the interface between the active layer and the interlayer compared to the PNDITphN-based device. This difference in surface energy also correlates with the previously observed variations in trap density from the carrier dynamics analysis.

Universality Verification. To verify the general effect of these two polymers on device performance, both PNDITphN and PNDITphN-Br were employed with active layers of PM6:Y6 and PM6:D18:L8-BO. The chemical structures of donors and acceptors are depicted in Figure S11. As shown in Figure S12 and Table 3, compared to the PCE of 17.22% achieved by PNDITphN-Br-based OSC devices, devices using PNDITphN with the PM6:Y6 active layer achieved a maximum PCE of 17.78%, which is among one of the highest PCEs of devices based on the PM6:Y6 active layer. The higher PCE of PNDITphN-based devices is attributed to a higher average FF and J_{SC} . When ternary devices with an active layer of PM6:D18:L8-BO were fabricated, the results followed the same trend. Devices based on PNDITphN exhibited a higher PCE of 18.84% compared to 18.36% for PNDITphN-Br-based devices, in line with a higher average FF of 79.39% and a J_{SC} of 26.59 mA cm⁻². These findings demonstrate that the neutral side chain-based PNDITphN CIM is more conducive to efficient charge transport, resulting in higher FF and PCE.

Device Photostability. In order to verify the effect of CIMs on device photostability, devices based on different CIMs were tested under continuous irradiation with AM 1.5 G standard sunlight and 365 nm UV light, respectively. As shown

in Figure 6a, the device efficiency of the PFN-Br-based device decreased to 80% of the initial value after experiencing about 80 h of sunlight irradiation. Compared with PFN-Br, the corresponding device photostability of PNDITF3N is improved and reduced to 80% after the light exposure duration is extended to 195 h. Notably, PNDITphN with the replacement of the fluorene unit by the benzene unit showed the best photostability, which could still maintain 80% of its initial efficiency after undergoing 400 h of light exposure. To further investigate the relation of V_{OC} , J_{SC} , FF, and the CIMs, we analyzed in detail the trend of V_{OC} , J_{SC} , and FF changes with light exposure time, with the results presented in Figure S13. It is shown that both V_{OC} and J_{SC} of the three devices remain above 90%, while the degree of change in FF is the most significant as the light exposure time extends. After approximately 260 h of light exposure, the FF of PNDITphN retains 88% of its initial value, while those of PFN-Br and PNDITF3N only retain about 80% of their initial values. The results indicate that the photostability of the device can be effectively enhanced by adjusting the structure of the conjugated main chain of interface materials, and this result is consistent with the photostability of the material, as shown in previous absorption spectroscopy. Moreover, as shown in Figure 6b, compared with PFN-Br, the devices based on PNDITF3N and PNDITphN exhibit significantly better UV stability, and the devices based on PNDITphN also exhibit relatively better photostability, proving the effectiveness of the material design.

In addition, we also tested the storage stability of the device, and the results are shown in Figure S14. The device efficiency still maintained more than 88% of its initial value after more than 1700 h of storage in the glovebox.

CONCLUSION

In summary, we synthesized two polymer-based CIMs, PNDITphN and PNDITphN-Br, by the direct arylation polycondensation method. These polymers exhibit a good ability to tune the WF of the electrode and excellent electron transport properties, thereby improving the efficiency of OSCs. As a result, the PNDITphN- and PNDITphN-Br-based binary OSCs achieved maximum PCEs of 18.39% and 17.78%, respectively, which are higher than 15.48% for devices using PFN-Br. PNDITphN-based devices exhibit relatively higher efficiency because of their face-on molecular packing, more uniform surface morphology, and stronger interfacial contact with the active layer. Therefore, ternary devices using PNDITphN achieved a PCE of 18.84%, higher than 18.36% for devices using PNDITphN-Br. Moreover, compared with PFN-Br and PNDITF3N, PNDITphN-based devices exhibit superior photostability, which could maintain 80% of their initial efficiency after undergoing 400 h of light exposure, demonstrating the effectiveness of the material design strategy. This work provides an effective approach to obtain cathode interlayer materials with high efficiency and stability by a direct arylation polycondensation method through a main-chain modulation strategy.

EXPERIMENTAL SECTION

Synthesis of PNDITphN. NDI-EH, M4, potassium carbonate, pivalic acid, and Pd₂(dba)₃ were combined at a certain rate in a 15 mL sealed tube, and the mixture was purged with argon twice. Dry chlorobenzene was added under an argon atmosphere. The reaction mixture was stirred at 90 °C for 72 h. After cooling down to room

temperature, the reactant mixture was poured into MeOH, forming of the dark green precipitate. The precipitate was filtered and successively extracted with methanol, acetone, hexane, and chloroform by Soxhlet extraction. The chloroform fraction was concentrated and precipitated into methanol. The precipitate was collected and dried under vacuum overnight to give the dark green polymer.

Synthesis of PNDITphN-Br. PNDITphN was dissolved in CHCl₃, followed by the addition of bromoethane. The mixture was stirred at 50 °C for 4 days; once some precipitates appeared, some methanol was added to dissolve them. Then the solvent was removed under reduced pressure, and the crude product was dissolved in methanol. The solution was filtered with a 0.45 μm PTFE filter, concentrated, and precipitated from ethyl acetate. The solid was collected and dried under vacuum overnight to give the dark green polymer.

■ ASSOCIATED CONTENT

SI Supporting Information

The Supporting Information is available free of charge at <https://pubs.acs.org/doi/10.1021/acs.chemmater.5c01203>.

General materials and methods, synthetic procedures and characterizations of monomers, polymerization procedures, ¹H and ¹³C NMR spectra, GPC data, TGA and DSC results, carrier dynamics analysis, and OSC device characterization results (PDF)

■ AUTHOR INFORMATION

Corresponding Authors

Haoran Tang – Institute of Polymer Optoelectronic Materials and Devices, State Key Laboratory of Luminescent Materials and Devices, Guangdong Basic Research Center of Excellence for Energy & Information Polymer Materials, South China University of Technology, Guangzhou 510641, P. R. China; orcid.org/0000-0002-0963-7230; Email: mstanghaoran@scut.edu.cn

Fei Huang – Institute of Polymer Optoelectronic Materials and Devices, State Key Laboratory of Luminescent Materials and Devices, Guangdong Basic Research Center of Excellence for Energy & Information Polymer Materials, South China University of Technology, Guangzhou 510641, P. R. China; orcid.org/0000-0001-9665-6642; Email: msfhuang@scut.edu.cn

Authors

Haiyang Zhao – Institute of Polymer Optoelectronic Materials and Devices, State Key Laboratory of Luminescent Materials and Devices, Guangdong Basic Research Center of Excellence for Energy & Information Polymer Materials, South China University of Technology, Guangzhou 510641, P. R. China

Zixin Huang – Institute of Polymer Optoelectronic Materials and Devices, State Key Laboratory of Luminescent Materials and Devices, Guangdong Basic Research Center of Excellence for Energy & Information Polymer Materials, South China University of Technology, Guangzhou 510641, P. R. China

Zhibin Li – Institute of Polymer Optoelectronic Materials and Devices, State Key Laboratory of Luminescent Materials and Devices, Guangdong Basic Research Center of Excellence for Energy & Information Polymer Materials, South China University of Technology, Guangzhou 510641, P. R. China

Yuanqing Bai – Institute of Polymer Optoelectronic Materials and Devices, State Key Laboratory of Luminescent Materials and Devices, Guangdong Basic Research Center of Excellence for Energy & Information Polymer Materials, South China University of Technology, Guangzhou 510641, P. R. China

Hui Li – Institute of Polymer Optoelectronic Materials and Devices, State Key Laboratory of Luminescent Materials and Devices, Guangdong Basic Research Center of Excellence for Energy & Information Polymer Materials, South China University of Technology, Guangzhou 510641, P. R. China

Chunchen Liu – Institute of Polymer Optoelectronic Materials and Devices, State Key Laboratory of Luminescent Materials and Devices, Guangdong Basic Research Center of Excellence for Energy & Information Polymer Materials, South China University of Technology, Guangzhou 510641, P. R. China; orcid.org/0000-0002-5830-1805

Kai Zhang – Institute of Polymer Optoelectronic Materials and Devices, State Key Laboratory of Luminescent Materials and Devices, Guangdong Basic Research Center of Excellence for Energy & Information Polymer Materials, South China University of Technology, Guangzhou 510641, P. R. China; orcid.org/0000-0003-2931-7135

Complete contact information is available at:

<https://pubs.acs.org/doi/10.1021/acs.chemmater.5c01203>

Author Contributions

*H. Z. and Z. H. contributed equally to this work.

Notes

The authors declare the following competing financial interest(s): The authors have filed the patent application.

■ ACKNOWLEDGMENTS

This work was financially supported by National Natural Science Foundation of China (No. 52433012) and China Postdoctoral Science Foundation (No. 2023M741201 and No. 2024T170286).

■ REFERENCES

- Heeger, A. J. 25th Anniversary Article: Bulk Heterojunction Solar Cells: Understanding the Mechanism of Operation. *Adv. Mater.* **2014**, *26*, 10–28.
- Liu, Y.; Cole, M. D.; Jiang, Y.; Kim, P. Y.; Nordlund, D.; Emrick, T.; Russell, T. P. Chemical and Morphological Control of Interfacial Self-Doping for Efficient Organic Electronics. *Adv. Mater.* **2018**, *30* (15), 1705976.
- Huang, F.; Bo, Z. -S.; Geng, Y.-H.; Wang, X.-H.; Wang, L. -X.; Ma, Y. -G.; Hou, J.-H.; Hu, W.-P.; Pei, J.; Dong, H.-L.; et al. Study on Optoelectronic Polymers: An Overview and Outlook. *Acta Polym. Sin* **2019**, *50*, 988–1046.
- Tang, H.; Liang, Y.; Liu, C.; Hu, Z.; Deng, Y.; Guo, H.; Yu, Z.; Song, A.; Zhao, H.; Zhao, D.; Zhang, Y.; Guo, X.; Pei, J.; Ma, Y.; Cao, Y.; Huang, F. A solution-processed n-type conducting polymer with ultrahigh conductivity. *Nature* **2022**, *611*, 271–277.
- Zhong, Z.; Chen, S.; Zhao, J.; Xie, J.; Zhang, K.; Jia, T.; Zhu, C.; Jing, J.; Liang, Y.; Hong, L.; et al. Non-Halogen Solvent Processed Binary Organic Solar Cells with Efficiency of 19% and Module Efficiency Over 15% Enabled by Asymmetric Alkyl Chain Engineering. *Adv. Energy Mater.* **2023**, *13* (39), 2302273.
- Tang, H.; Cai, H.; Zhao, H.; Liu, Z.; Tan, R.; Huang, F. A Solution-Processed n-Type Conducting Polymer Without Side Chains Formed via Nonmetal-Participated Polymerization and in Situ n-Doping. *CCS Chem.* **2023**, *5*, 2534–2544.
- Jing, J.; Dou, Y.; Chen, S.; Zhang, K.; Huang, F. Solution sequential deposited organic photovoltaics: From morphology control to large-area modules. *eScience* **2023**, *3*, 100142.
- Guan, S.; Li, Y.; Xu, C.; Yin, N.; Xu, C.; Wang, C.; Wang, M.; Xu, Y.; Chen, Q.; Wang, D.; et al. Self-Assembled Interlayer Enables High-Performance Organic Photovoltaics with Power Conversion Efficiency Exceeding 20%. *Adv. Mater.* **2024**, *36* (25), 2400342.

- (9) Sun, Y.; Wang, L.; Guo, C.; Xiao, J.; Liu, C.; Chen, C.; Xia, W.; Gan, Z.; Cheng, J.; Zhou, J.; Chen, Z.; Zhou, J.; Liu, D.; Wang, T.; Li, W. π -Extended Nonfullerene Acceptor for Compressed Molecular Packing in Organic Solar Cells To Achieve over 20% Efficiency. *J. Am. Chem. Soc.* **2024**, *146*, 12011–12019.
- (10) Jiang, Y.; Sun, S.; Xu, R.; Liu, F.; Miao, X.; Ran, G.; Liu, K.; Yi, Y.; Zhang, W.; Zhu, X. Non-fullerene acceptor with asymmetric structure and phenyl-substituted alkyl side chain for 20.2% efficiency organic solar cells. *Nat. Energy* **2024**, *9*, 975–986.
- (11) Chen, Z.; Ge, J.; Song, W.; Tong, X.; Liu, H.; Yu, X.; Li, J.; Shi, J.; Xie, L.; Han, C.; et al. 20.2% Efficiency Organic Photovoltaics Employing a π -Extension Quinoxaline-Based Acceptor with Ordered Arrangement. *Adv. Mater* **2024**, *36* (33), 2406690.
- (12) Song, J.; Li, C.; Ma, H.; Han, B.; Wang, Q.; Wang, X.; Wei, D.; Bu, L.; Yang, R.; Yan, H.; et al. Optimizing Double-Fibril Network Morphology via Solid Additive Strategy Enables Binary All-Polymer Solar Cells with 19.50% Efficiency. *Adv. Mater.* **2024**, *36*, 2406922.
- (13) Xie, J.; Zhao, J.; Zhou, Z.; Zhang, K.; Yu, J.; Zhu, C.; Huang, F. Multifunctional ternary semitransparent organic solar cell module with area above 100 cm² and average visible transmittance above 30%. *Energy Environ. Sci.* **2024**, *17*, 7681–7690.
- (14) Huang, Q.; Jing, J.; Zhang, K.; Chen, Y.; Song, A.; Liu, Z.; Huang, F. Simultaneous improvement of efficiency and stability of inverted organic solar cell via composite hole transport layer. *J. Mater. Chem. A* **2022**, *10*, 23973–23981.
- (15) Bai, Y.; Hong, L.; Dou, Y.; Zhu, S.; Tang, H.; Liu, D.; Cao, Y.; Chen, J.; Chen, S.; Shao, L.; Hu, Z.; Tang, D.; Zhang, K.; Su, S.-J.; Liu, C.; Huang, F. C-Shape or S-Shape? The Molecular Geometry Control of Fused-Ring Nonfullerene Acceptors for Lower Energy Loss in Organic Solar Cells. *ACS Energy Lett.* **2024**, *9*, 1786–1795.
- (16) Liang, Y.; Zhang, D.; Wu, Z.; Jia, T.; Lüer, L.; Tang, H.; Hong, L.; Zhang, J.; Zhang, K.; Brabec, C. J.; Li, N.; Huang, F. Organic solar cells using oligomer acceptors for improved stability and efficiency. *Nat. Energy* **2022**, *7*, 1180–1190.
- (17) Cai, P.; Song, C.; Lei, S.; Yu, K.; Ding, L.; Wang, D.; Chen, G.; Peng, H.; Li, B.; Wang, X.; Xiao, B.; Yang, R. A robust and thickness-insensitive hybrid cathode interlayer for high-efficiency and stable inverted organic solar cells. *J. Mater. Chem. A* **2023**, *11*, 18723–18732.
- (18) Jiang, H.; Liang, Q.; Guo, H.; Zhang, A.; Wang, X.; Tang, Z.; Bo, Z. All Roads Lead to Rome: Isomers with Divergent Cathode Modification Mechanisms toward Ohmic Contact. *J. Am. Chem. Soc.* **2024**, *146*, 30262–30271.
- (19) Yang, R.; Tian, J.; Liu, W.; Wang, Y.; Chen, Z.; Russell, T. P.; Liu, Y. Nonconjugated Self-Doped Polymer Zwitterions as Efficient Interlayers for High Performance Organic Solar Cells. *Chem. Mater.* **2022**, *34*, 7293–7301.
- (20) Zhu, C.; Tian, J.; Liu, W.; Duan, Y.; Song, Y.; You, Z.; Wang, X.; Li, N.; Zhan, X.; Russell, T. P.; Liu, Y. Batch-Reproducible and Thickness-Insensitive Mesopolymer Zwitterion Interlayers for Organic Solar Cells. *ACS Energy Lett.* **2023**, *8*, 2689–2698.
- (21) You, Z.; Song, Y.; Liu, W.; Wang, W.; Zhu, C.; Duan, Y.; Liu, Y. Diazabicyclic Electroactive Ionenes for Efficient and Stable Organic Solar Cells. *Angew. Chem. Int. Ed.* **2023**, *62* (23), No. e202302538.
- (22) Zhao, H.; Dou, Y.; Chen, S.; Tang, H.; Bai, Y.; Tan, R.; Zhang, K.; Liu, C.; Huang, F. Novel In Situ Self-Doping Cathode Interlayer Materials with Thickness-Insensitivity for High-Efficiency Organic Solar Cells. *Chem. Mater.* **2023**, *35*, 8695–8705.
- (23) Wang, Z.; Wang, H.; Du, M.; Lai, X.; He, F.; Guo, Q.; Guo, Q.; Tang, A.; Sun, X.; Zhou, E. Naphthodithiophene Diimide (NDTI)-Based Cathode Interlayer Material Enables 19% Efficiency Binary Organic Solar Cells. *Adv. Funct. Mater.* **2024**, *34* (12), 2313240.
- (24) Luo, X.; Yu, J.; Tang, H.; Cai, H.; Xiong, W.; Zhang, K.; Huang, F.; Cao, Y. Self-doped conjugated polymers with electron-deficient quinone units for enhanced electron transport in highly efficient organic solar cells. *FlexMater* **2024**, *1*, 105–115.
- (25) Zheng, H.; Hu, L.; Hu, X.; Li, H.; Quan, J.; Jin, Y.; Yin, X.; Song, J.; Su, Z.; Zhou, D.; Li, Z. Designing thickness-insensitive cathode interlayers via constructing noncovalently conformational locks for highly efficient non-fullerene organic solar cells. *J. Mater. Chem. A* **2024**, *12*, 2413–2422.
- (26) Xia, D.; Wang, J.; Chen, X.; Zhao, C.; Fang, J.; Xie, Q.; Zhang, Y.; Luo, C.; Hu, Z.; Jiang, X.; Li, R.; You, S.; Xie, Y.; Jiang, L.; Li, W. Electron-Transporting Polymer with Perfluoroalkyl Spacer Enables Efficient and Stable Non-Fullerene Organic Solar Cells. *Macromolecules* **2024**, *57*, 8374–8382.
- (27) Wang, X.; Liang, Q.; Zhang, A.; Wei, N.; Jiang, H.; Cheng, Y.; Fang, H.; Li, S.; Lu, H.; Li, W.; Bo, Z. Amide-Based Cathode Interfacial Layer with Dual-Modification Mechanisms Enables Stable Organic Solar Cells with High Efficiency Achieving 20%. *J. Am. Chem. Soc.* **2025**, *147*, 9261–9272.
- (28) Tang, H.; Bai, Y.; Zhao, H.; Qin, X.; Hu, Z.; Zhou, C.; Huang, F.; Cao, Y. Interface Engineering for Highly Efficient Organic Solar Cells. *Adv. Mater.* **2024**, *36* (16), 2212236.
- (29) Suemori, K.; Yokoyama, M.; Hiramoto, M. Electrical shorting of organic photovoltaic films resulting from metal migration. *J. Appl. Phys.* **2006**, *99* (3), 036109.
- (30) Lee, K.; Kim, J. Y.; Park, S. H.; Kim, S. H.; Cho, S.; Heeger, A. J. Air-Stable Polymer Electronic Devices. *Adv. Mater.* **2007**, *19*, 2445–2449.
- (31) Xin, Y.; Liu, H.; Dong, X.; Xiao, Z.; Wang, R.; Gao, Y.; Zou, Y.; Kan, B.; Wan, X.; Liu, Y.; Chen, Y. Multiarmed Aromatic Ammonium Salts Boost the Efficiency and Stability of Inverted Organic Solar Cells. *J. Am. Chem. Soc.* **2024**, *146*, 3363–3372.
- (32) Jiang, Y.; Sun, L.; Jiang, F.; Xie, C.; Hu, L.; Dong, X.; Qin, F.; Liu, T.; Hu, L.; Jiang, X.; Zhou, Y. Photocatalytic effect of ZnO on the stability of nonfullerene acceptors and its mitigation by SnO₂ for nonfullerene organic solar cells. *Mater. Horiz.* **2019**, *6*, 1438–1443.
- (33) Waldauf, C.; Morana, M.; Denk, P.; Schilinsky, P.; Coakley, K.; Choulis, S. A.; Brabec, C. J. Highly efficient inverted organic photovoltaics using solution based titanium oxide as electron selective contact. *Appl. Phys. Lett.* **2006**, *89* (23), 233517.
- (34) Xiang, Y.; Xu, B.; Li, Y. Solution-Processed Semiconductor Materials as Cathode Interlayers for Organic Solar Cells. *Adv. Sci* **2023**, *10* (34), 2304673.
- (35) Zhang, Z.-G.; Qi, B.; Jin, Z.; Chi, D.; Qi, Z.; Li, Y.; Wang, J. Perylene diimides: A thickness-insensitive cathode interlayer for high performance polymer solar cells. *Energy Environ. Sci.* **2014**, *7*, 1966–1973.
- (36) Yao, J.; Qiu, B.; Zhang, Z.-G.; Xue, L.; Wang, R.; Zhang, C.; Chen, S.; Zhou, Q.; Sun, C.; Yang, C.; et al. Cathode engineering with perylene-diimide interlayer enabling over 17% efficiency single-junction organic solar cells. *Nat. Commun.* **2020**, *11* (1), 2726.
- (37) Liu, M.; Jiang, Y.; Liu, D.; Wang, J.; Ren, Z.; Russell, T. P.; Liu, Y. Imidazole-Functionalized Imide Interlayers for High Performance Organic Solar Cells. *ACS Energy Lett.* **2021**, *6*, 3228–3235.
- (38) Zhao, K.; Ye, L.; Zhao, W.; Zhang, S.; Yao, H.; Xu, B.; Sun, M.; Hou, J. Enhanced efficiency of polymer photovoltaic cells via the incorporation of a water-soluble naphthalene diimide derivative as a cathode interlayer. *J. Mater. Chem. C* **2015**, *3*, 9565–9571.
- (39) Kang, Q.; Ye, L.; Xu, B.; An, C.; Stuard, S. J.; Zhang, S.; Yao, H.; Ade, H.; Hou, J. A Printable Organic Cathode Interlayer Enables over 13% Efficiency for 1-cm² Organic Solar Cells. *Joule* **2019**, *3*, 227–239.
- (40) Yu, Y.; Wang, J.; Cui, Y.; Chen, Z.; Zhang, T.; Xiao, Y.; Wang, W.; Wang, J.; Hao, X.-T.; Hou, J. Cost-Effective Cathode Interlayer Material for Scalable Organic Photovoltaic Cells. *J. Am. Chem. Soc.* **2024**, *146*, 8697–8705.
- (41) Huang, F.; Wu, H.; Wang, D.; Yang, W.; Cao, Y. Novel Electroluminescent Conjugated Polyelectrolytes Based on Polyfluorene. *Chem. Mater.* **2004**, *16*, 708–716.
- (42) Liu, S.; Zhong, C.; Zhang, J.; Duan, C.; Wang, X.; Huang, F. A novel crosslinkable electron injection/transporting material for solution processed polymer light-emitting diodes. *Sci. China: Chem.* **2011**, *54*, 1745–1749.
- (43) Liu, S.; Zhang, K.; Lu, J.; Zhang, J.; Yip, H.-L.; Huang, F.; Cao, Y. High-Efficiency Polymer Solar Cells via the Incorporation of an

Amino-Functionalized Conjugated Metallopolymer as a Cathode Interlayer. *J. Am. Chem. Soc.* **2013**, *135*, 15326–15329.

(44) He, Z.; Zhang, C.; Xu, X.; Zhang, L.; Huang, L.; Chen, J.; Wu, H.; Cao, Y. Largely Enhanced Efficiency with a PFN/Al Bilayer Cathode in High Efficiency Bulk Heterojunction Photovoltaic Cells with a Low Bandgap Polycarbazole Donor. *Adv. Mater.* **2011**, *23*, 3086–3089.

(45) He, Z.; Zhong, C.; Su, S.; Xu, M.; Wu, H.; Cao, Y. Enhanced power-conversion efficiency in polymer solar cells using an inverted device structure. *Nat. Photonics* **2012**, *6*, 591–595.

(46) Wu, Z.; Sun, C.; Dong, S.; Jiang, X.-F.; Wu, S.; Wu, H.; Yip, H.-L.; Huang, F.; Cao, Y. n-Type Water/Alcohol-Soluble Naphthalene Diimide-Based Conjugated Polymers for High-Performance Polymer Solar Cells. *J. Am. Chem. Soc.* **2016**, *138*, 2004–2013.

(47) Liu, H.; Xin, Y.; Suo, Z.; Yang, L.; Zou, Y.; Cao, X.; Hu, Z.; Kan, B.; Wan, X.; Liu, Y.; Chen, Y. Dipole Moments Regulation of Biposphonic Acid Molecules for Self-assembled Monolayers Boosts the Efficiency of Organic Solar Cells Exceeding 19.7%. *J. Am. Chem. Soc.* **2024**, *146*, 14287–14296.

(48) Li, Y.; Wang, L.; Fu, H.; Zheng, Q. Piperazine-Functionalized Arylene Diimides as Electron Transport Layers for High-Efficiency and Stable Organic Solar Cells. *Adv. Funct. Mater.* **2025**, *35* (15), 2419342.

(49) Wang, Z.; Wang, H.; Yang, L.; Du, M.; Gao, L.; Guo, Q.; Zhou, E. Selenophene-fused Perylene Diimide-Based Cathode Interlayer Enables 19% Efficiency Binary Organic Solar Cells via Stimulative Charge Extraction. *Angew. Chem., Int. Ed.* **2024**, *63* (37), No. e202404921.

(50) Liu, L.; Tang, S.; Liu, M.; Xie, Z.; Zhang, W.; Lu, P.; Hanif, M.; Ma, Y. Photodegradation of Polyfluorene and Fluorene Oligomers with Alkyl and Aromatic Disubstitutions. *J. Phys. Chem. B* **2006**, *110*, 13734–13740.

(51) Grisorio, R.; Allegretta, G.; Mastrorilli, P.; Suranna, G. P. On the Degradation Process Involving Polyfluorenes and the Factors Governing Their Spectral Stability. *Macromolecules* **2011**, *44*, 7977–7986.

(52) Balanda, P. B.; Ramey, M. B.; Reynolds, J. R. Water-Soluble and Blue Luminescent Cationic Polyelectrolytes Based on Poly(p-phenylene). *Macromolecules* **1999**, *32*, 3970–3978.

(53) Henson, Z. B.; Zhang, Y.; Nguyen, T.-Q.; Seo, J. H.; Bazan, G. C. Synthesis and Properties of Two Cationic Narrow Band Gap Conjugated Polyelectrolytes. *J. Am. Chem. Soc.* **2013**, *135*, 4163–4166.

(54) Yu, Y.; Cui, Y.; Zhang, T.; Chen, Z.; Xiao, Y.; Wang, W.; Yang, Y.; Yang, N.; Hou, J. An Interfacial Material with Low Trap Density Enables Efficient Organic Photovoltaic Cells for Multi-Scene Applications. *Adv. Funct. Mater.* **2023**, *33* (49), 2306095.

(55) Zhang, Y.; Chen, J.; Yang, J.; Fu, M.; Cao, Y.; Dong, M.; Yu, J.; Dong, S.; Yang, X.; Shao, L.; et al. Sensitive SWIR Organic Photodetectors with Spectral Response Reaching 1.5 μm . *Adv. Mater.* **2024**, *36* (41), 2406950.

(56) Street, R. A.; Yang, Y.; Thompson, B. C.; McCulloch, I. Capacitance Spectroscopy of Light Induced Trap States in Organic Solar Cells. *J. Phys. Chem. C* **2016**, *120*, 22169–22178.

(57) Chen, Z.; Li, Q.; Tang, H.; Wen, J.; Zhong, Y.; Zhang, J.; Han, K.; Liu, Y. Dominant Face-On Oriented Perylene-Diimide Interlayers for High-Performance Organic Solar Cells. *Angew. Chem. Int. Ed.* **2025**, *64* (18), No. e202424502.

(58) Kozbial, A.; Li, Z.; Conaway, C.; McGinley, R.; Dhingra, S.; Vahdat, V.; Zhou, F.; D'Urso, B.; Liu, H.; Li, L. Study on the Surface Energy of Graphene by Contact Angle Measurements. *Langmuir* **2014**, *30*, 8598–8606.



CAS BIOFINDER DISCOVERY PLATFORM™

**PRECISION DATA
FOR FASTER
DRUG
DISCOVERY**

CAS BioFinder helps you identify targets, biomarkers, and pathways

Unlock insights

CAS
A Division of the
American Chemical Society